2017

Utilizing Ground-Based LIDAR Measurements to Aid Autonomous Airdrop Systems

Martin Cacan
Georgia Institute of Technology

Edward Scheuermann
Georgia Institute of Technology

Michael Ward
Georgia Institute of Technology

Mark Costello
Georgia Institute of Technology

Nathan Slegers
George Fox University, nslegers@georgefox.edu

Utilizing ground-based LIDAR measurements to aid autonomous airdrop systems

Martin Cacan[1], Edward Scheuermann[1], Michael Ward[2], Mark Costello[1,2] and Nathan Slegers[3]

Abstract

Uncertainty in atmospheric winds represents one of the primary sources of landing error in airdrop systems. In this work, a ground-based LIDAR system samples the wind field at discrete points above the target and transmits real-time data to approaching autonomous airdrop systems. In simulation and experimentation, the inclusion of a light detection and ranging (LIDAR) system showed a maximum of 40% improvement over unaided autonomous airdrop systems. Wind information nearest ground level has the largest impact on improving accuracy.

Keywords

Autonomous, guided airdrop system, LIDAR, parafoil, wind field mapping

Date received: 12 March 2015; accepted: 18 August 2015

Introduction

Airdrop systems have been used for decades to deliver supplies in remote or forward operating locations where ground-based delivery systems are limited. Conventional unguided airdrop systems employing circular parachutes require complex payload release algorithms and accurate drop scheduling to land near the target.[1] Autonomous airdrop systems employ ram-air parachutes which can penetrate atmospheric winds and use control logic in concert with sensor feedback to land at a specified target. Control methods for parafoils are typically accomplished with left and right trailing edge deflection, yielding lateral control authority.

With all airdrop systems, an accurate estimate of the wind profile between the release point and the ground is essential for accurate landings. Modern guided airdrop systems typically use GPS feedback to obtain continuous wind estimates and plan their approach trajectories accordingly.[2–9] Onboard estimation simplifies airdrop operations since an additional device is not required but does not yield a wind estimate at altitudes below the system.[10,11] Significant landing errors can result if the winds near the ground differ significantly from the wind estimates used to plan the systems approach path. Yakimenko et al.[12] showed that deviations in the wind below an altitude of 100 m can shift the landing point of a guided airdrop system by over 100 m from the target.

There are several techniques commonly employed for measuring wind velocity including pitot tubes, hot wire systems, cup anemometers, and various laser-based systems. Pitot systems and cup anemometers are rugged and relatively low cost but provide a two-dimensional wind measurement at a single point.[13,14] On the other hand, laser-based systems such as a light detection and ranging (LIDAR) unit are expensive but provide three-dimensional estimates of the wind field at numerous points along the laser beams.[14–16]

This work examines the use of a ground-based LIDAR unit to provide real-time atmospheric wind data in the vicinity of the landing target to aid in approach planning for guided airdrop systems. The paper begins with a description of the data processing algorithm for using LIDAR measurements to construct an atmospheric wind field profile. This is followed by a brief description of parafoil autonomous control logic incorporating wind profile data. In order to make use of this feedback information, new

[1]Woodruff School of Mechanical Engineering, Georgia Institute of Technology, Atlanta, USA
[2]Guggenheim School of Aerospace Engineering, Georgia Institute of Technology, Atlanta, USA
[3]College of Engineering, George Fox University, Newberg, USA

Corresponding author:
Mark Costello, Georgia Institute of Technology, 270 Ferst Drive, Atlanta, GA 30332, USA.
Email: mark.costello@ae.gatech.edu

guidance logic is created to interface with the atmospheric wind measurements from the LIDAR unit. Simulation and flight experiment results are reported in a variety of atmospheric wind conditions showcasing the ability of ground-based LIDAR measurements to improve autonomous airdrop system landing accuracy. A trade study is also presented to analyze the benefits from including a LIDAR unit in autonomous airdrop operations.

Wind estimation with ground-based LIDAR

Figure 1 provides a schematic of a ground-based LIDAR unit emitting laser beams to estimate the atmospheric wind field in a region around a landing location. Each laser beam records the component of the atmospheric wind velocity along the beam at a discrete set of locations along the beam, called range gates. The orientation of an arbitrary beam is depicted in Figure 2, where the kth laser beam is defined by an azimuth ψ_k and elevation θ_k angle.

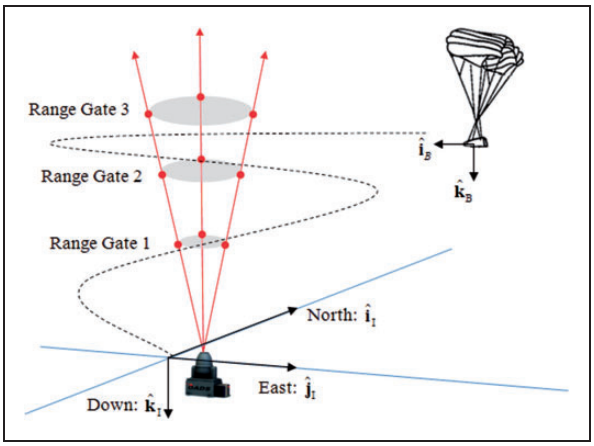

Figure 1. Concept showing ground-based LIDAR system used in conjunction with an autonomous parafoil.
LIDAR: light detection and ranging..

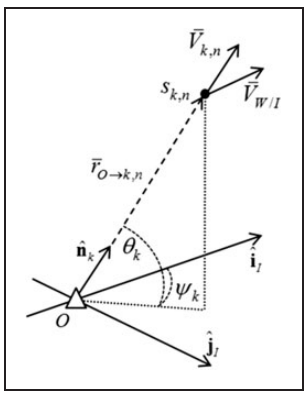

Figure 2. LIDAR laser beam schematic.
LIDAR: light detection and ranging.

The coordinates of the nth range gate along beam k relative to the LIDAR system located at the origin of the inertial coordinate frame are given by equations (1) to (3)

$$\mathbb{C}(\bar{r}_{O\to k,n}) = \begin{Bmatrix} x_{k,n} \\ y_{k,n} \\ z_{k,n} \end{Bmatrix} \tag{1}$$

$$\begin{aligned} r_{k,n} &= |\bar{r}_{O\to k,n}|, \\ k &= \operatorname{atan2}(y_{k,n}, x_{k,n}), \\ \theta_k &= \sin^{-1}\left(\tfrac{-z_{k,n}}{r_{k,n}}\right) \end{aligned} \tag{2}$$

$$\begin{aligned} x_{k,n} &= r_{k,n}\cos(\theta_k)\cos(\psi_k) \\ y_{k,n} &= r_{k,n}\cos(\theta_k)\sin(\psi_k) \\ z_{k,n} &= r_{k,n}\sin(\theta_k) \end{aligned} \tag{3}$$

The directional unit vector of the kth laser beam is defined by its orientation

$$\mathbb{C}(\hat{\mathbf{n}}_k) = \begin{Bmatrix} \hat{\mathbf{n}}_{kx} \\ \hat{\mathbf{n}}_{ky} \\ \hat{\mathbf{n}}_{kz} \end{Bmatrix} = \begin{Bmatrix} \cos(\theta_k)\cos(\psi_k) \\ \cos(\theta_k)\sin(\psi_k) \\ \sin(\theta_k) \end{Bmatrix} \tag{4}$$

At an altitude band of interest, it is assumed that the three atmospheric wind velocity measure numbers are constant throughout the sampled airspace

$$\mathbb{C}(\bar{V}_{W/I}) = \begin{Bmatrix} V_{Wx} \\ V_{Wy} \\ V_{Wz} \end{Bmatrix} \tag{5}$$

Measurements from the LIDAR unit can be constructed as a dot product between the atmospheric wind velocity vector and the laser beam unit vector. For three noncoplanar beams, a unique relationship exists between the three orthogonal components of the wind vector and the three nonorthogonal components of the LIDAR velocity measurements (V_1, V_2, V_3)

$$\begin{Bmatrix} V_1 \\ V_2 \\ V_3 \end{Bmatrix} = \begin{Bmatrix} \bar{V}_{W/I}\cdot\hat{\mathbf{n}}_1 \\ \bar{V}_{W/I}\cdot\hat{\mathbf{n}}_2 \\ \bar{V}_{W/I}\cdot\hat{\mathbf{n}}_3 \end{Bmatrix} = \begin{bmatrix} n_{1x} & n_{1y} & n_{1z} \\ n_{2x} & n_{2y} & n_{2z} \\ n_{3x} & n_{3y} & n_{3z} \end{bmatrix} \begin{Bmatrix} V_{Wx} \\ V_{Wy} \\ V_{Wz} \end{Bmatrix} = [H] \begin{Bmatrix} V_{Wx} \\ V_{Wy} \\ V_{Wz} \end{Bmatrix} \tag{6}$$

The LIDAR measurement and wind estimation arrangement used for the work described here is shown in Figure 3. The LIDAR beams are equally spaced on a cone around the vertical direction. Measurements are obtained from each beam at specified range gates. With samples from three different

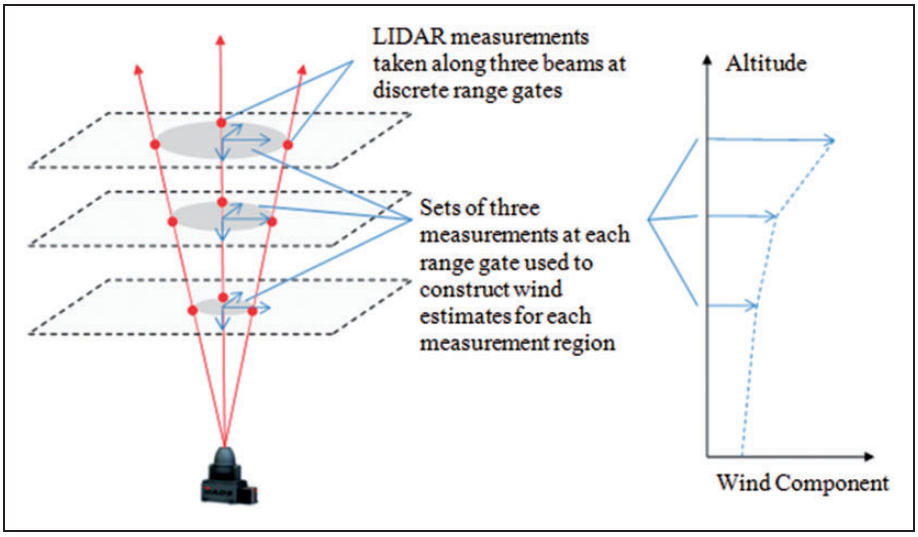

Figure 3. Constructing wind profile from LIDAR measurements.[17]
LIDAR: light detection and ranging.

beams at the same altitude, a constant wind velocity is estimated at that altitude by solving equation (6) for the unknown atmospheric velocity components (V_{Wx}, V_{Wy}, V_{Wz}) along the north, east, and down directions, respectively. These wind estimates are used to construct an altitude-dependent profile of the atmospheric wind over the LIDAR unit. The atmospheric wind velocity field is linearly interpolated at a specific height above ground to yield an estimate at any height within the field. In order to account for changes in the measured wind field with time, a first-order filter is used to update the measured data resulting in a relatively smooth changes in the wind profile.

Onboard guidance, navigation, and control (GNC) algorithm

The purpose of the GNC algorithm is to perform path planning, estimate relevant state and atmospheric conditions, and track the desired path using parafoil control inputs. The details of each are outlined below and are based on the current practice used for guided airdrop systems. The unique aspect of this GNC algorithm is the ability to incorporate estimated wind profile information gathered by the LIDAR system.

A guidance algorithm

The guidance algorithm has inputs from measured and estimated state and atmospheric conditions and plans how to accurately reach the landing target. The guidance algorithm used here makes use of a wind-based reference frame (WF). This reference frame translates horizontally with the local wind field and rotates such that the $\hat{i}_{WF}$ axis is aligned with the downwind direction expected at ground level. A visual representation of the WF related to the inertial frame is presented in Figure 4. This method was initially introduced by

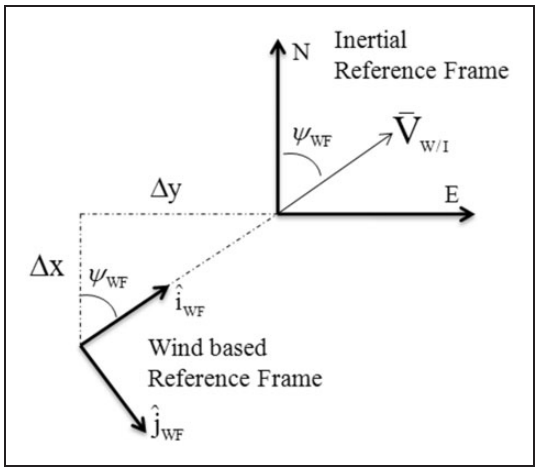

Figure 4. Visual representation of the wind-based reference frame. It is offset from the inertial origin by an amount $(\Delta x, \Delta y)$ and rotated to align with the ground wind direction.

Goodrick and Murphy[18] and more recently by Jann,[19] who shifted the wind field horizontally, $(\Delta x, \Delta y)$, based upon the integral of the wind profile and decent rate

$$\begin{aligned} \Delta x &= \int_0^h \frac{V_{Wx}(z)}{\dot{z}(z)} dz \\ \Delta y &= \int_0^h \frac{V_{Wy}(z)}{\dot{z}(z)} dz \end{aligned} \tag{7}$$

At any instant in time, average atmospheric wind velocity parameters $(\tilde{V}_{Wx}, \tilde{V}_{Wy})$ can be defined as the average atmospheric wind velocity in the horizontal plane (in the $\hat{i}_I$ and $\hat{j}_I$ directions, respectively) from the current system altitude to the ground

$$\begin{aligned} \tilde{V}_{Wx} &= \frac{1}{h}\int_0^h V_{Wx}(z) dz \\ \tilde{V}_{Wy} &= \frac{1}{h}\int_0^h V_{Wy}(z) dz \end{aligned} \tag{8}$$

The formulas in equation (7) can be simplified by using the average atmospheric wind velocity parameters in the inertial x and y directions calculated in equation (8). Additionally, the vertical decent rate for the system, ($\dot{z}$) is assumed to be constant. While variations are expected due to atmospheric updrafts and sinks, over the course of the entire flight, it is realistic to assume they average to zero. The average atmospheric wind velocity parameters are generated using measurements of the wind velocity from the LIDAR unit at multiple altitudes above ground level. The location of the parafoil and payload system in the WF can be defined based on the inertial location of the system and expected drift due to wind buffeting the system

$$\begin{aligned} x_{WF} &= x_I + \tfrac{h}{\dot{z}}\tilde{V}_{Wx} \\ y_{WF} &= y_I + \tfrac{h}{\dot{z}}\tilde{V}_{Wy} \end{aligned} \tag{9}$$

It is important to note that vertical atmospheric winds are not used to shift the WF as thermals and local sinks have a high amount of spatial variability and often do not persist throughout the entire flight. The orientation of the wind-based reference is based on the ground anemometer attached to the LIDAR unit and aligns the $\hat{i}_{WF}$ with the ground wind direction (V^G_{Wx}, V^G_{Wy}). Note that a first-order filter is applied to the ground anemometer measurements in order to prevent rapid rotation of the WF based on slight variations in ground wind conditions

$$\psi_{WF} = \text{atan2}\left(V^G_{Wy}, V^G_{Wx}\right) \tag{10}$$

LIDAR estimates over a range of altitudes in concert with ground wind measurements from an anemometer provide sufficient data to compute accurate average atmospheric wind field estimates. This wind field information accounts for all future wind conditions in which the airdrop system will fly. This permits the effect of atmospheric winds on the landing location to be determined accurately and enables efficient steering to be determined as a perturbation maneuver superimposed on the atmospheric wind effect. This is more accurate than conventional strategies where the wind magnitude and direction estimated at altitude is assumed to be constant from the system altitude to the ground. Conventional strategies offer no foresight to the guidance logic and actually provide slightly lagged estimates based on the nature of the estimation filter.

During flight, the guidance algorithm defines waypoints in the WF for the system to track. Given the initial location and heading, along with a final position and heading (defined by the waypoint) a path is created to achieve these goals using time optimal Dubins paths with a constant turning radius. Here, Dubins path planning works to minimize the flight distance with three maneuver elements: initially turning at a maximum rate in the direction of the waypoint; flying straight to approach the waypoint; and when near the waypoint, turning to match desired heading.[6,19,20]

The guidance algorithm is decomposed into four stages (initialization, loiter, approach, and flare) which enable accurate landing.

1. Initialization phase

During this phase, initial estimates for the airspeed of the parafoil and payload system and horizontal wind components are computed. This provides initial conditions for the extended Kalman filter to estimate the state vector during the flight. At the onset of initialization, a constant differential brake input is commanded to induce a constant system turn rate. This maneuver exposes the vehicle heading and airspeed to different angles of the horizontal atmospheric winds. These velocities sum either constructively or destructively to generate an oscillating ground track velocity measured by GPS. The amplitude variation can be attributed to the horizontal wind components and solved for using the least squares algorithm in equation (11). During this period, both horizontal wind velocities and system airspeed are assumed constant

$$\begin{bmatrix} \dot{x}_1^{GPS} - \mu_{\dot{x}} & \dot{y}_1^{GPS} - \mu_{\dot{y}} \\ \vdots & \vdots \\ \dot{x}_N^{GPS} - \mu_{\dot{x}} & \dot{y}_N^{GPS} - \mu_{\dot{y}} \end{bmatrix} \begin{Bmatrix} V_{Wx} \\ V_{Wy} \end{Bmatrix} = \frac{1}{2} \begin{bmatrix} \left(V_1^2\right)^{GPS} - \mu_{V^2} \\ \vdots \\ \left(V_N^2\right)^{GPS} - \mu_{V^2} \end{bmatrix} \tag{11}$$

Here, N is the number of data points collected across the initialization period and the μ_A terms represent the average value of A over the data set. The airspeed of the parafoil and payload system, V_0, can be solved by subtracting the estimated wind from the measured components of the ground track velocity which are then averaged over the initialization period as presented in equation (12)

$$\begin{gathered} V_{0,i} = \sqrt{\left(\dot{x}_i^{GPS} - V_{Wx}\right)^2 + \left(\dot{y}_i^{GPS} - V_{Wy}\right)^2} \\ V_0 = \mu_{V_0} \end{gathered} \tag{12}$$

Further detail on this work can be found in Ward et al.[10]

2. Loiter phase

After the initialization phase, the system can define the WF, or a frame that accounts for the drift of the aircraft due to the wind. This is constantly updated as the wind changes as a function of space and time. This is captured by either the onboard extended Kalman filter or uploaded to the onboard flight computer from the LIDAR unit ground station. The goal of

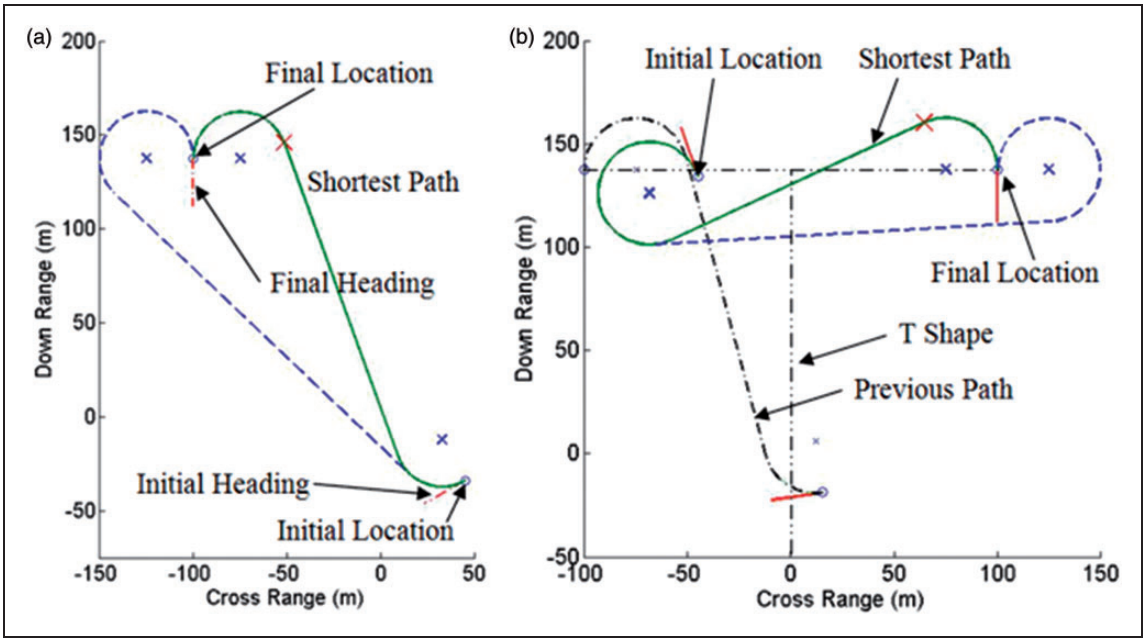

Figure 5. Visualization of Dubins path planning (a) immediately after initialization and (b) after reaching the first waypoint.

the loiter period is to maintain the vehicle's location near the target in preparation for final approach. This is accomplished by assigning loiter targets at specified distance downwind and specified distance perpendicular to a line drawn straight downwind from the target (in the WF) for the system to track. These reference lines form the "T approach" and are shown in Figure 5(b) as dashed black lines. Using these targets ensures the system maintains relative position just downwind of the target such that it can transition to final approach and fly up the stem of the "T" in order to land directly into the wind at the target.

Path planning between waypoints is done through Dubins paths which are comprised of an initial and final turn of fixed turn radius and a straight line segment tangent to both circles. Four path options are available by turning left or right from the current location and heading and approaching the final location and heading with a left or right turn. The final location is based upon the loiter targets of the "T" and the final heading is always chosen to be upwind in order to prevent significant downwind drift of the system. The guidance algorithm analyzes the four paths and selects the shortest feasible path which is illustrated by a solid line in Figure 5 while one of three suboptimal paths is presented by a dashed line.

When the parafoil and payload system leaves the initialization phase (Figure 5(a)), it plans an approach to the first T waypoint. The algorithm identifies that the shortest path is a right turn followed by a left turn when near the target. These circles allow the initial and final heading requirements to be met and ensure the system always turns upwind. The control algorithm then works to track this desired path. Due to any potential shifts in the wind, this geometry would rotate in the inertial frame in order to keep the stem of the T pointed downwind.

In Figure 5(b), the parafoil and payload system has reached the first waypoint (defined by a circular space around the waypoint) and switches to track the next waypoint. The new path chosen by the autopilot does not take it directly through the previous waypoint as precisely reaching it is not necessary. This flexibility is removed when tracking the final landing point. Again, the algorithm finds the shortest Dubins path to go from the current location to the final location while ensuring that the paths are tangent to the initial and final headings.

During the entire loitering period, the altitude required to reach the target from the current location is computed constantly (h_{req}). The instantaneous distance to the target, L, is defined by the arc of the circle required to turn from the current heading to point at the target and the straight line between the end of this turning circle and the target

$$L = |\mathrm{d}\psi|R + ||\bar{x}_1 - \bar{x}_T|| \tag{13}$$

Here, $d\psi$, R, $\bar{x}_1$, and $\bar{x}_T$ are the change in heading, turning radius, the coordinates at the end of the turn, and the coordinates of the landing target. This is then converted into the required height based on the glide slope

$$h_{req} = L\frac{\dot{z}}{V_0} \tag{14}$$

When the current altitude drops below h_{req}, the system switches into the approach phase.

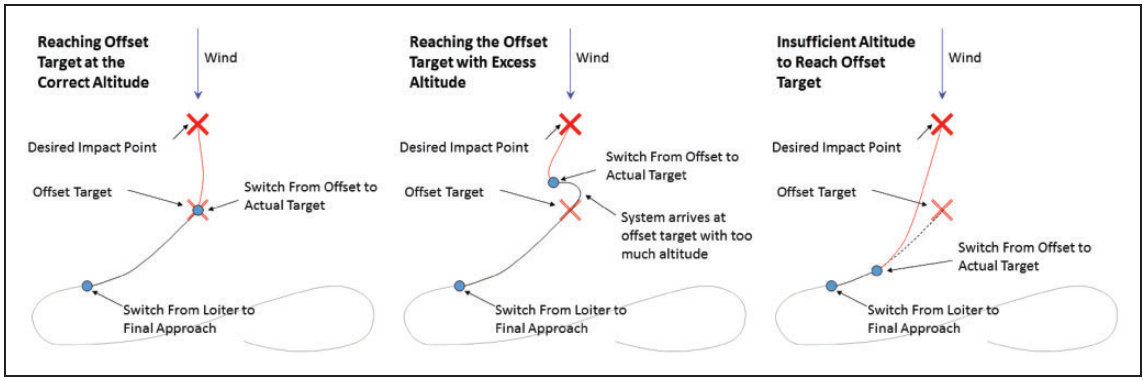

Figure 6. Cases outlining two-stage final approach methodologies.[21]

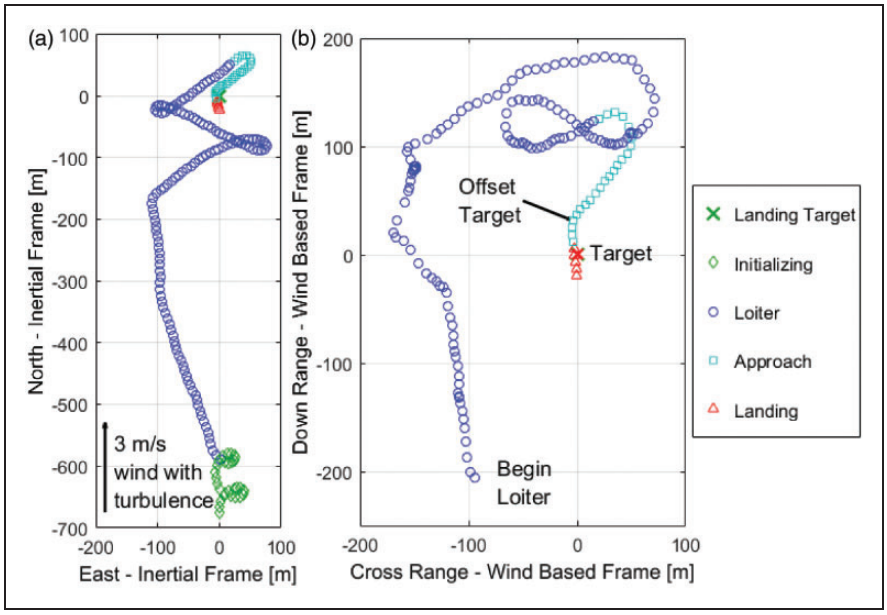

Figure 7. Sample simulated flight trajectory of the guided airdrop system in the (a) inertial frame and (b) wind-based frame.

3. Approach phase

This section deviates from the figure eight holding pattern and attempts to fly along the stem of the T upwind toward the target. An offset target is introduced that is downwind of the desired impact point which ensures that the end of the trajectory is a straight line segment pointed into the wind. Some adjustments can be made to the trajectory if the system is going to reach the offset target with too much or too little altitude. If the system has too much altitude, the system flies a portion of a circle until the excess altitude is lost and the current height equals the high required to reach the landing point. If the system has too little altitude, the offset target is abandoned early, and the system flies directly to the landing point. These three cases are demonstrated in Figure 6.

4. Flare phase

The goal of the landing maneuver is to minimize the kinetic energy of the system just before impact. Below a preset altitude threshold the system is commanded to fly upwind, even if it means turning away from the target. Just before impact, full symmetric brake is then applied to flare the canopy just short of stall in order to slow the airspeed of the airdrop system. An example flight history is shown in Figure 7 to highlight all four stages of the guidance algorithm. The simulation was initialized with the airdrop system located above the landing zone in the WF. On the left, the simulation results are plotted in the inertial frame, as such, the discussed T-shape approach is continuously shifting to keep a constant offset distance in the WF. On the right, the simulation

results are plotted in the WF, showing the fixed T-shape approach before landing short of the target.

Navigation algorithm

After the initialization phase where initial estimates of the atmospheric wind velocities and assumed constant airspeed are found, two Kalman filters are used to update estimates and filter measurement noise. Measured data are $(x, y, z)^{GPS}$ and $(\dot{x}, \dot{y}, \dot{z})^{GPS}$ where the derivatives are found using finite difference approximation given the sampling rate. A stationary Kalman filter estimates the position (x, y, z), velocity $(\dot{x}, \dot{y}, \dot{z})$. The navigation estimate for the x component is given by equation (15)

$$\begin{bmatrix} x_{i+1}^{nv} \\ \dot{x}_{i+1}^{nv} \end{bmatrix} = \begin{bmatrix} x_i^{nv} + \dot{x}_i^{nv}\mathrm{d}t \\ \dot{x}_i^{nv} \end{bmatrix} + \begin{bmatrix} G_{x0} \\ G_{x2} \end{bmatrix} \left(x_{i+1}^{GPS} - \left(x_i^{nv} + \dot{x}_i^{nv}\mathrm{d}t\right)\right) + \begin{bmatrix} G_{x2} \\ G_{x3} \end{bmatrix} \left(\dot{x}_{i+1}^{GPS} - \dot{x}_i^{nv}\right) \tag{15}$$

Here, the Kalman gains, G_{xi} are calculated and programmed onto the guidance computer before flight. The same logic is used to estimate the y and z positions and velocities. An extended Kalman filter is used to estimate horizontal wind, heading, and heading rate. This filter varies from the previous in that the Kalman filter gain, G_{KF}, is calculated real time and depends on current vehicle heading angle and airspeed. Further detail on the navigation algorithm, including calculation of the Kalman gain, is presented in Ward[21]

$$\begin{bmatrix} W_{x,i+1}^{nv} \\ W_{y,i+1}^{nv} \\ {}_{i+1}^{nv} \\ \dot{\psi}_{i+1}^{nv} \end{bmatrix} = \begin{bmatrix} W_{x,i}^{nv} \\ W_{y,i}^{nv} \\ {}_{i}^{nv} + \dot{\psi}_i^{nv}\mathrm{d}t \\ \dot{\psi}_i^{nv} \end{bmatrix} + G_{KF}\left(\begin{bmatrix} \dot{x}_{i+1}^{GPS} \\ \dot{y}_{i+1}^{GPS} \end{bmatrix} - \begin{bmatrix} W_{x,i}^{nv} + V_0\cos\left(\psi_i^{nv}\right) \\ W_{y,i}^{nv} + V_0\sin\left(\psi_i^{nv}\right) \end{bmatrix}\right) \tag{16}$$

As the guidance computer now has an accurate estimate of system parameters, it can work to control certain states to land accurately at the target.

Control algorithm

The airdrop system is controlled using left and right trailing edge brake deflection. This increases drag on a specific side of the canopy, inducing a lateral turning moment allowing the guidance algorithm to track a commanded heading angle. The steering is done through a PI controller. The proportional component is nonlinear to reduce the control error due to small heading error. This method is the current standard for parafoil and payload control. No incidence angle or longitudinal control was used although it has been shown to improve landing accuracy.[21,22] Based on the current waypoint target supplied by the guidance algorithm and the estimated location of the system in the WF, a commanded heading value is generated. This is compared to the actual heading filtered by the navigation algorithm and mapped to a commanded turn rate, $\dot{\psi}_C$

$$\Delta\psi = \psi_C - {}^{nv} \tag{17}$$

$$\Delta\psi_{ratio} = \frac{\Delta\psi}{\Delta\psi_{max}} \tag{18}$$

$$\dot{\psi}_C = \begin{cases} \dot{\psi}_{max} & \text{if} \Delta\psi_{ratio} \geqslant 1 \\ -\dot{\psi}_{max} & \text{if} \Delta\psi_{ratio} \leqslant 1 \\ \dot{\psi}_{max}\Delta\psi_{ratio}\sqrt{|\Delta\psi_{ratio}|} & \text{else} \end{cases} \tag{19}$$

From the desired turn rate, asymmetric brake deflection, δa_C, is determined based on an actuator gain and bias term. The gain is a design parameter, and the asymmetric brake bias is computed from the integral control logic and allows the airdrop system to fly straight

$$\delta a_C = G_{\delta a}\dot{\psi}_C + \delta a_{bias} \tag{20}$$

It should be noted that δa_C is a parameter that varies in the span $[-1, 1]$ signifying the maximum turning effort in both left and right directions. This asymmetric brake parameter is then converted into the individual brake deflection of the left and right trailing edge, δl_C and δr_C, respectively

$$\begin{aligned} \delta l_C &= \delta b_C - 0.5\delta a_C \\ \delta r_C &= \delta b_C + 0.5\delta a_C \end{aligned} \tag{21}$$

Here, symmetric brake level, δb_C, is fixed at 0.4. To achieve a desired turn rate, each actuator only needs to act over half of the needed brake differential, leading to faster actuator response. Also, this method tends to have a lesser impact on the nominal airspeed of the airdrop system during turning, making path planning computationally more efficient. Only under flare in the final stage of the guidance algorithm, does the symmetric brake level change in order to slow the system to near stall prior to landing. Additionally note that based on these definitions, δl_C and δr_C are mapped from 0 to 1 which is the minimum to maximum range of the brake actuators.

Simulation models

Parafoil and payload model

Figure 8 shows a schematic of a parafoil and payload system. With the exception of movable parafoil brakes, the parafoil canopy is considered to be a fixed shape. The combined system of the parafoil

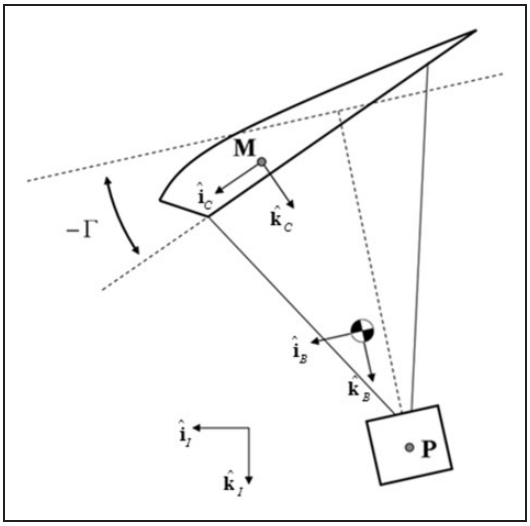

Figure 8. Parafoil and payload schematic.

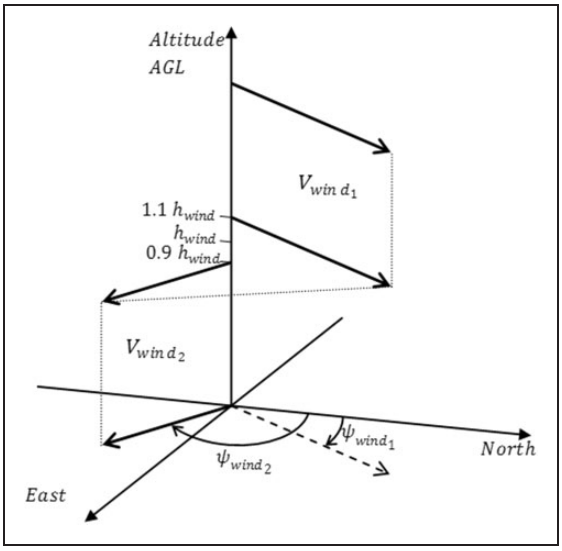

Figure 9. Horizontal wind shear profile.[17]

canopy and the payload is represented by a six degrees of freedom, rigid-body model, defined by three inertial position components of the total system mass center as well as the three Euler orientation angles. The canopy aerodynamic forces and moments are computed about the canopy aerodynamic center (point M in Figure 8). The transformation from the body frame (frame B in Figure 8) to the canopy reference frame (frame C in Figure 8) is defined by a single axis rotation in pitch by the canopy incidence angle, Γ. The equations of motion for this six degree of freedom parafoil and payload representation have been derived previously and validated through flight testing.[10,11,21]

Simple shear wind field model

Low-frequency, large-scale components of the wind are generated by a horizontal wind profile which is variable between flights and constant during a particular flight. This wind field, presented in Figure 9, is meant to capture large-scale, slowly varying features like wind shear. In a simple and concise manner, this wind model captures the nature of atmospheric wind fields close to the ground. By statistically varying the parameters that comprise the model, a rich variety of physical scenarios can be constructed.

To capture high-frequency, small-scale components of the wind, a discrete implementation of the Dryden turbulence model was used.[23] Gust velocities and angular rate components are computed for all three axes by driving discrete filters with unit-variance, independent white noise signals. A sample wind field created by the simple shear model with and without Dryden turbulence is shown in Figure 10. The turbulence is altitude dependent, but has the general form of high-frequency, small amplitude oscillations that slowly drift around the underlying simple shear wind model.

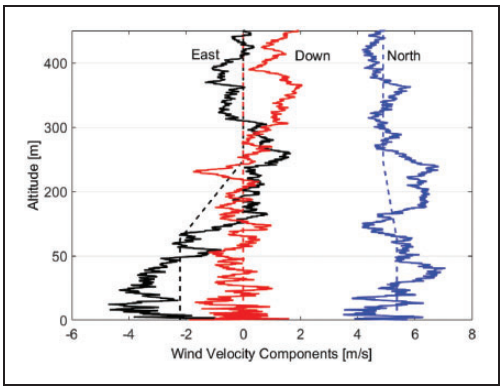

Figure 10. Example wind profile showing underlying simple shear model (dashed lines) and actual wind modified by Dryden turbulence (solid lines).

Results

Simulated and experimental results are obtained by using a small-scale parafoil and payload system shown in Figure 11. Simulation model parameters were identified through extensive system identification techniques yielding an accurate computational model for initial validation of the improved guidance logic.[11,21] The test vehicle uses high torque servos with extended arms to actuate the trailing edge brakes for lateral control. An autopilot is mounted onboard the payload and contains a sensor suite including a barometric altimeter and GPS receiver, a flight computer for executing autonomous control algorithms, onboard memory for data logging, and a 2.4 GHz wireless link to the LIDAR unit via a ground station computer. This small-scale system was designed to provide an elegant alternative to full size airdrop system testing which require guided payloads to be dropped from manned aircraft. Relevant weight and system geometry specifications (presented in Table 1)

Figure 11. Parafoil and payload system during gliding flight.

Table 1. Mass and geometry parameters of the small-scale parafoil and payload system.

Parameter	Value	Units
Total mass	2.87	kg
Span (b)	1.88	m
Chord (c)	0.8	m
Wing area	1.5	m^2
Wing loading	1.9	kg/m^2
Airspeed	7.2	m/s

were chosen to select a wing loading that would match the turn rate dynamics of a full size airdrop system.[24]

The LIDAR wind field measurement unit is shown in Figure 12 mounted in the rear of a pickup truck for transportation and experimental testing. The unit uses a set of three laser beams to provide three unique measurements of the wind field at a range of altitudes to generate a vertically varying wind profile. An ultrasonic anemometer mounted to the base of the LIDAR unit measures horizontal ground wind magnitude and direction. The LIDAR unit sampled the wind field at a 1 Hz rate and sent the data through a serial connection to a ground station computer to be relayed up to the parafoil and payload system. Relevant geometric parameters of the LIDAR system are listed in Table 2 and were used to define the LIDAR unit in the simulation model.

To present an initial comparison between a conventional system using onboard wind estimation and the LIDAR-aided system, each system is simulated to fly through identical wind fields. It is important to note that the conventional system uses identical guidance logic as presented in "Onboard guidance, navigation, and control (GNC) algorithm" section except that the WF must be calculated solely with onboard estimates and is unaware of winds at lower altitudes. Figures 13 and 14 illustrate sample trajectories and wind estimates, respectively, for the conventional

Figure 12. LIDAR unit mounted in the rear of a pickup truck with base station laptop used for experimental testing. LIDAR: light detection and ranging.

Table 2. Geometry parameters for the LIDAR wind field measurement unit.

Parameter	Value	Units
θ	75	deg
	[0,120,240]	deg
h	[160,220,280,340,400,500]	ft

LIDAR: light detection and ranging.

and LIDAR-aided system. At altitude, there is a 4 m/s wind flowing north which transitions to a 2 m/s wind flowing southeast below 75 m. The LIDAR-aided system trajectory shows significant variation from the conventional system trajectory due to the advanced knowledge of the wind shear. The LIDAR

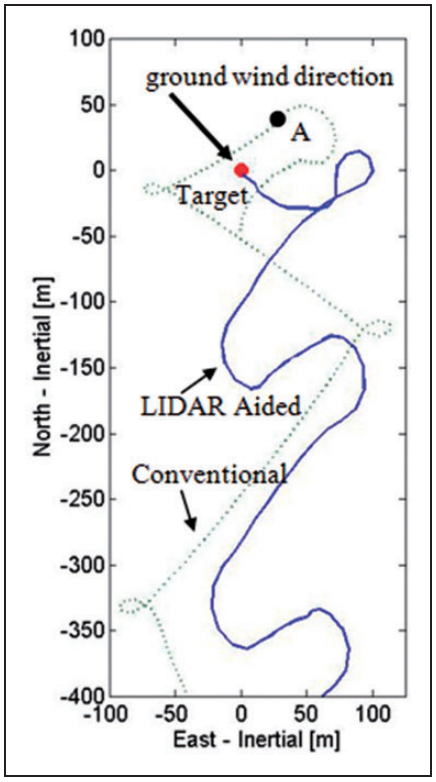

Figure 13. Simulated results comparing the LIDAR-aided system and conventional system trajectories.
LIDAR: light detection and ranging.

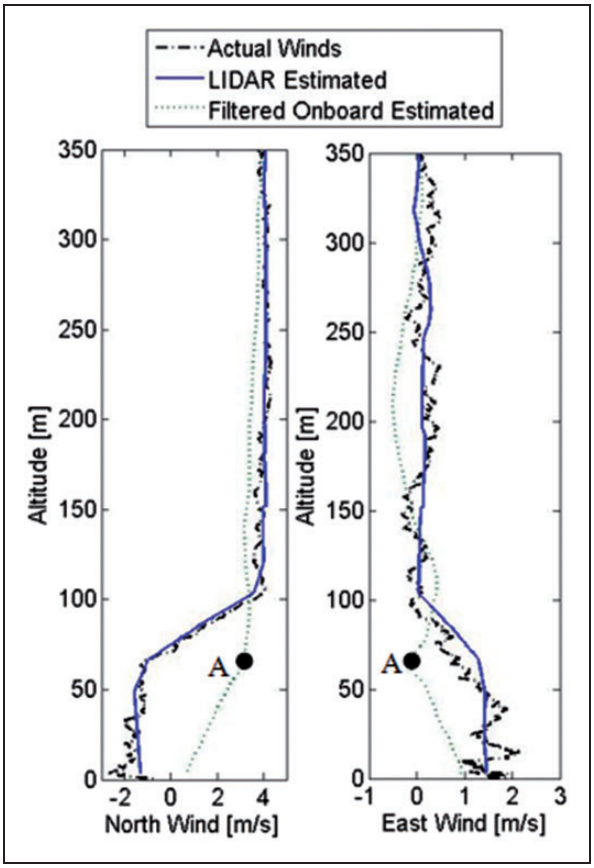

Figure 14. North and east wind estimates used by the guidance algorithm for an airdrop system using onboard estimation or LIDAR wind field measurements.
LIDAR: light detection and ranging.

system stays downwind (with respect to the ground wind) of the target, allowing the system to land accurately into the wind. The conventional system does not react to the wind shear until point A in Figure 13 at which point it moves around the target to get downwind based on the current estimate. When the conventional system reaches final approach, the wind estimates do not accurately reflect the actual conditions due to the lagged nature of the estimation. The system stops tracking the intended target and points in the direction assumed to be upwind (east of southeast) since landing into the wind is prioritized during final approach. During this final period, the system is blown sideways by the actual wind causing the system trajectory to have a final trajectory that trails south of the intended target.

To fully test the effect of LIDAR atmospheric wind estimates on landing accuracy, a series of Monte Carlo simulations were conducted. Three sets of simulations were conducted. The first analyzed the effectiveness of a LIDAR to improve landing accuracy of a parafoil and payload system flying in a wind field with a large shear component. In the second, the configuration of the LIDAR unit is analyzed by studying the landing accuracy against the number and location of altitudes being measured by the unit. Lastly, the time dependence of the LIDAR profile estimate is analyzed by the addition of low-frequency gusts to the wind model.

A comparison of the landing accuracy using different wind estimation techniques

The simple wind shear profile shown in Figure 9 is used for this set of simulations with the addition of Dryden turbulence. All of the wind field parameters were varied according to a random distribution over the ranges listed in Table 3. One thousand simulated landing trajectories were generated for each of three cases: (1) fully autonomous landing using only the onboard wind estimate, (2) landing with wind estimates provided by the ground-based LIDAR at 1 Hz, and (3) landing with perfect knowledge of the entire wind profile. Landing dispersion results of these case studies are shown in Figures 15 to 17, with circles denoting 50% circular error probable (CEP) (also called the median miss distance) and 90% CEP displayed. The CEP directly signifies the radius of a circle, centered at the origin, at which 50% (or 90%) of the landings fell within. Note that the axes of the landing dispersion plots in Figures 15 to 17 are for downwind and crosswind directions, indicating that all landing points recorded in the inertial reference frame have been rotated into the WF. This implies that the wind is flowing from the bottom of

the figure to the top, and that the guided airdrop system lines up for approach at the top of the figure as it prepares to landing into the wind.

For the conventional system which uses only onboard wind estimation methods, overall landings statistics indicate a 50% CEP of 20.4 m and 90% CEP of 59.6 m. The landing dispersion shows clumped landings along the downwind axis with significant outliers in both crosswind and downwind directions. Misses in the downwind direction are primarily due to variations in system descent rate due to vertical winds which are not included in the guidance logic due to their spatial variability and changes in the ground wind magnitude from those at higher altitudes. Crosswind misses are attributed to incorrect wind direction estimates by the onboard system, causing over- or undershooting the target to result in a crosswind miss. Additionally, when the system is not properly aligned into the headwind, the ground winds induce a system sideslip velocity with respect to the inertial reference frame which can move the system off course. When the wind field has a low shear height, the GNC

Table 3. Wind shear parameters for Monte Carlo simulation.

Model parameter	Variation range
High altitude wind speed	0–6 m/s
Low altitude wind speed	0–6 m/s
High altitude wind heading	0°
Low altitude wind heading	0–360°
Height of wind shear	50–200 m
Release altitude	450 m

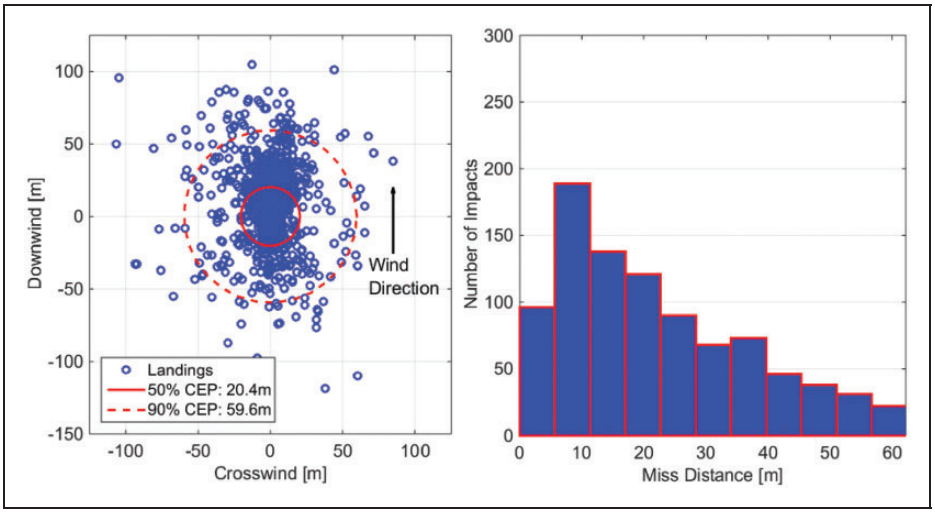

Figure 15. Simulated landing dispersion and histogram for a guided airdrop system conventional wind estimation technique.

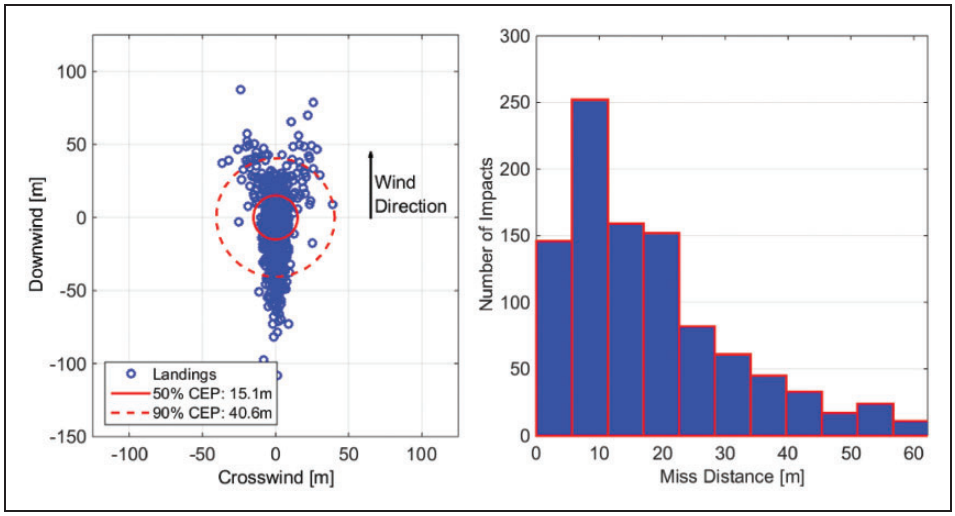

Figure 16. Simulated landing dispersion and histogram for a guided airdrop system provided LIDAR wind measurements. LIDAR: light detection and ranging.

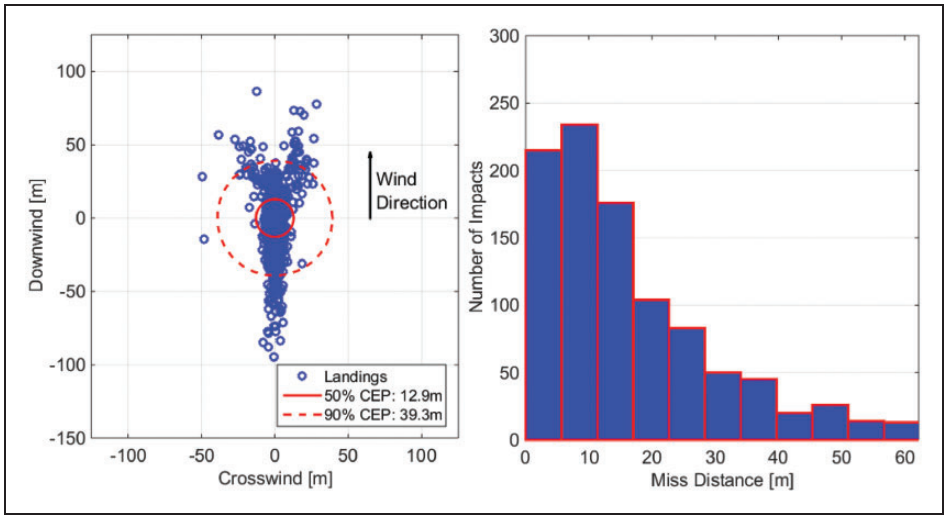

Figure 17. Simulated landing dispersion and histogram for a guided airdrop system provided true wind conditions.

logic has little time and altitude to account for the change resulting in more substantial miss distances.

With the addition of a LIDAR unit at the drop zone, accurate ground wind direction measurements from the anemometer significantly reduce the crosswind misses seen in the conventional system. Prior wind velocity information below the airdrop system's altitude improves the 50% CEP by 26% to 15.1 m. Misses in the crosswind direction are reduced dramatically due to a priori and accurate knowledge of the ground wind direction allowing the guidance algorithm to accurately rotate the WF for path planning (see equation (9)). Along the downwind axis, slight reductions in landing error can be noted due to better knowledge of ground wind magnitude but still exhibit significant variation out due to vertical wind disturbances. A slight "V" shape trend is noted in landing dispersion in Figure 16 which are short of the target (systems that land downwind). This is a result of the guidance logic rejecting the offset target and going directly for the desired ground target which was outlined previously in Figure 6 and related discussion (see "Insufficient Altitude to Reach Offset Target" case). The true wind case shows only partial improvement over the LIDAR-aided system with a 50% CEP of 12.9 m. This indicates that the LIDAR wind field measurements are of sufficient quality and density to produce an accurate reproduction of the true wind profile and that the control logic is robust to the error associated with the LIDAR measurements. Additional landing statistics for all configurations are presented in Table 4.

Table 4. Landing statistics for three landing cases.

Wind method	50% CEP (m)	Mean miss (m)	90% CEP (m)
Onboard estimation	20.4	27.3	59.6
LIDAR estimation	15.1	19.5	40.6
True wind	12.9	17.8	39.3

CEP: circular error probable; LIDAR: light detection and ranging.

LIDAR configuration study

As the benefit of atmospheric wind mapping has been shown to aid in the landing accuracy of guided airdrop systems, the range and density of the mapping is analyzed. Two LIDAR configuration trade studies were established to explore how increasing the wind profile map improves landing accuracy. The first parametric trade study involves a fixed interval of 50 m altitude between LIDAR atmospheric wind velocity estimates, starting at 0 m. The second parametric trade study fixes the maximum range of the LIDAR samples at 450 m and varies the number of equally spaced sample altitudes between the ground and maximum altitude. Both cases are illustrated in Figure 18. Note that a value of zero for the number of range gates signifies that LIDAR was not used and an onboard estimation technique was employed.

The simulated wind field for testing was a modified form of the simple shear model in order to add more variation in the wind field for the additional gates to register. A total of 1000 Monte Carlo simulations were run for each configuration, allowing for the extraction of relevant statistical data on the miss distance. The results of the simulations, shown in Figure 19, compare the CEP landing statistics for the two LIDAR configurations.

In each case studied, the 50% CEP miss statistics converge to approximately 14 m and the 90% CEP to approximately 40 m. The majority of the improved landing accuracy comes from the first range gate alone, corresponding to the ground wind measurement from the anemometer. For case A, an additional improvement was found in the 90% CEP when wind was measured at 50 m above the ground. Increasing

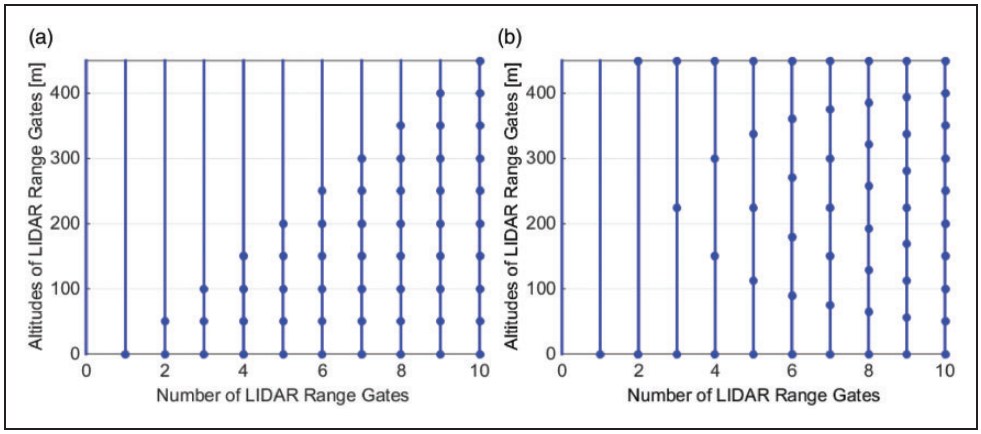

Figure 18. LIDAR configuration for the two parametric trade studies: (a) equal spacing and (b) fixed range. LIDAR: light detection and ranging.

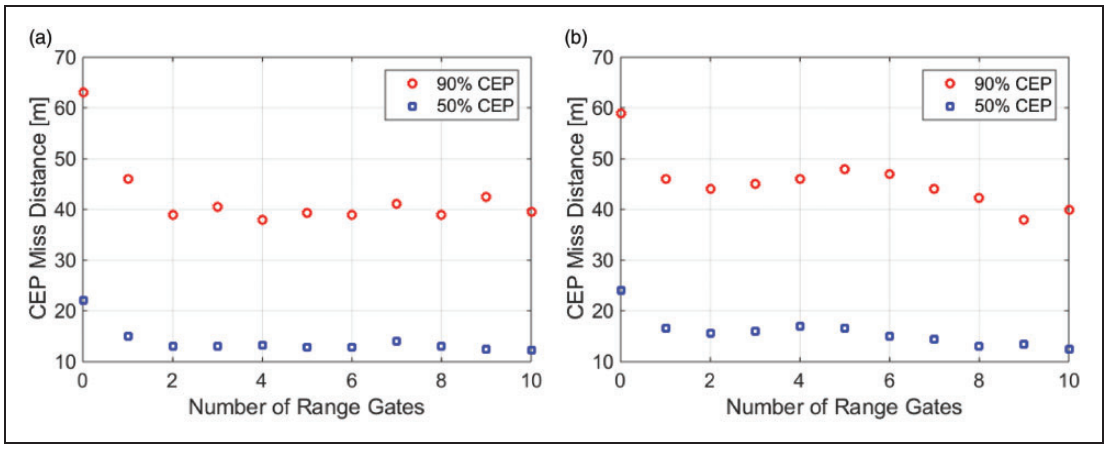

Figure 19. LIDAR configuration for the two parametric trade studies: (a) equal spacing and (b) fixed range. LIDAR: light detection and ranging.

the range gates to higher altitudes at similar intervals showed no improvement over the first two gates. Case B, however, showed a significantly higher 90% CEP miss value until the number of range gates reaches 8–10. These configurations, as seen by Figure 18, are representative of the lowest range gate dropping in altitude. This indicates that large miss distances, typically correlated to 90% CEP, can be significantly reduced by knowing the wind profile at or near the ground. Altitudes covering the final approach phase of the flight are most critical for improving landing accuracy of guided airdrop systems as there is the least amount of reserve altitude in which to correct for changes in the wind estimation.

Experimental validation

To validate the improvements of a LIDAR-aided system indicated by simulation results, the parafoil and payload system in Figure 11 is used to conduct a series of autonomous landings using either conventional guidance logic or LIDAR-aided guidance logic. For experimental testing, the small-scale system uses a rear mounted electric motor to provide thrust in order to climb to a simulated release altitude, at which point the power to the motor is cut and the guidance computer is engaged during gliding descent to steer the airdrop system to the landing target. Tests were conducted in rolling grassland terrain north of Atlanta, GA and flat desert terrain in Eloy, AZ. Tests were structured to switch between the conventional guidance logic and the improved guidance logic using LIDAR estimates of the atmospheric wind velocity in subsequent flights to ensure similar wind conditions between contrasted data sets.

In total, 54 autonomous landings were executed: 24 using conventional guidance logic and 30 using LIDAR-aided guidance logic. Landing dispersions and miss distance histograms for these two cases are presented in Figures 20 and 21. The conventional system has a 50% CEP of 24.7 m and 90% CEP of 48.5 m which is close to simulated results shown previously. The landing histogram also shows related trends with a slow taper in the number of landings that landed farther from the target. However, the landing dispersion shows a relatively distinct pattern

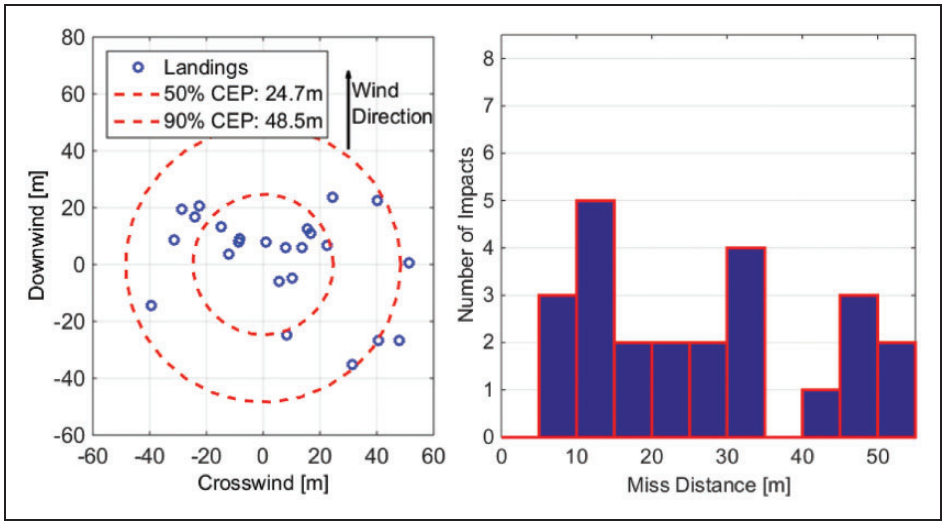

Figure 20. Experimental landing dispersion and histogram of a guided airdrop system using onboard wind estimation.

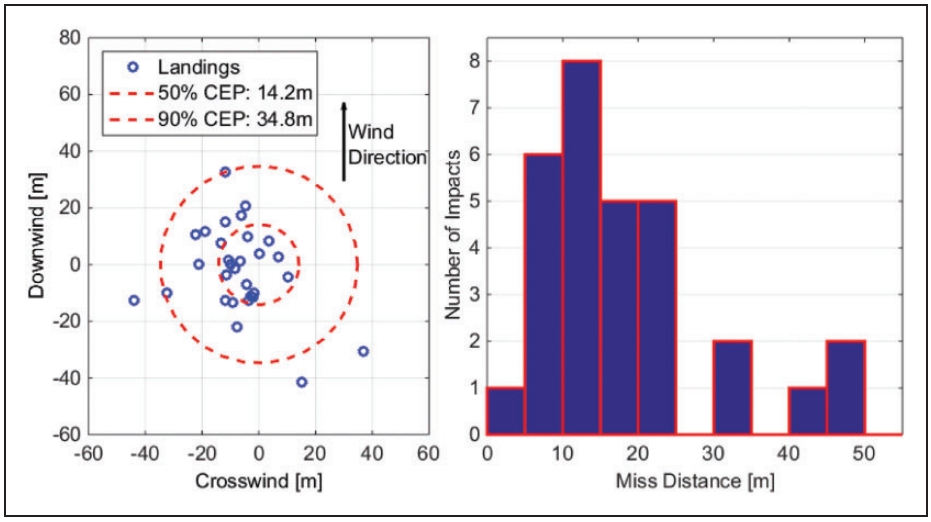

Figure 21. Experimental landing dispersion and histogram of a guided airdrop system LIDAR atmospheric wind measurements. LIDAR: light detection and ranging.

in comparison to simulated results. Most of the landings lie along the crosswind axis with any downwind miss also associated with a significant crosswind miss. Analysis of LIDAR wind field measurements and onboard wind estimates indicated that ground wind direction changed in a time varying nature, not solely based on altitude as assumed in the simple shear wind model used for simulation results. As a result, multiple cases show the system face into the low altitude wind during final approach only to have the wind direction change by the time impact occurred resulting in a crosswind landing.

Using the ground-based LIDAR unit to provide full wind field mapping, the 50% CEP landing accuracy improved by 43% to 14.2 m which compare very closely to simulated results. A significant reduction was noted in the crosswind miss due to low altitude and ground wind measurements provided by the LIDAR that gave the guidance system advanced knowledge of wind conditions. This also overcame time varying wind directional changes successfully due to the direct measurement of the wind field whereas the onboard wind estimation method tends to have a lagged identification. Overall landing results for the LIDAR-aided system align well with simulated results including the miss distance histogram which shows a significant peak in number of landings near the target.

Lastly, the simple shear wind field model and relevant parameters can be validated by processing LIDAR wind field measurements over the span of experimental flights recorded. LIDAR atmospheric wind data were analyzed to extract large-scale wind shear features by comparing the measured wind field to the simple shear wind model. While experimental data often showed more complex features such as

Table 5. Wind field statistics from experimental testing.

Parameter	Average	Minimum	Maximum
Wind at altitude (m/s)	3.16	0.9	6.1
Wind near ground (m/s)	1.63	0.3	4.4
Shear magnitude change (m/s)	1.53	−2.1	4.1
Shear direction change (°)	51.6	9.8	180.0
Shear altitude (m)	71.1	39.0	143.0

multiple or dynamic wind shears, primary trends were identified and listed in Table 5. Overall, the wind conditions from experimental testing aligned well with simulation wind conditions chosen, only showing much deviation in the shear altitude. This is interesting to note as it may be the primary reason for an increase in 50% CEP from simulated to experimental results for the conventional system. Lower shear altitudes present in experimental tests give the conventional system with onboard wind estimation less time to react to the wind shear which increases landing error. Note that change in wind shear magnitude is calculated by subtracting wind magnitude near ground level from the wind magnitude at the top of the atmospheric wind shear. This implies that the minimum value of −2.1 m/s in Table 5 is the result of ground winds being 2.1 m/s faster than the winds at altitude.

Conclusion

Landing accuracy of guided airdrop systems can be greatly improved using atmospheric wind field information in the vicinity of the intended landing area. Atmospheric wind field information was integrated into control logic in order to accurately define the location of a WF which accounts for the expected wind drift of the aerial vehicle between the current altitude and the ground. A detailed analysis of a conventional guidance algorithm in comparison to LIDAR-aided guidance logic indicated 26 and 43% reduction in miss distance in dynamic simulation and experimental flight tests, respectively. LIDAR wind measurements had the largest impact on reducing crosswind direction misses by providing forecasted wind conditions below the airdrop system's altitude. Most important was an accurate measurement and feedback of ground wind direction which actively reduced miss distance while improving payload survivability by ensuring the system landed into the wind. Lastly, a LIDAR wind field measurement configuration trade study showed that wind measurements at or near ground level had the largest impact on the landing accuracy of the guided airdrop system, particularly in the reduction of large miss distances.

Declaration of Conflicting Interests

The author(s) declared no potential conflicts of interest with respect to the research, authorship, and/or publication of this article.

Funding

The author(s) disclosed receipt of the following financial support for the research, authorship, and/or publication of this article: The authors would like to acknowledge the support of the Natick Soldier Research Development and Engineering Center (NSRDEC) Airdrop Technology Team.

References

1. Ewing E, Bixby H and Knacke T. *Recovery systems design guide*. CA: Tech. Rep. Irving Industries Inc., 1978.
2. Calise AJ and Preston D. Swarming/flocking and collision avoidance for mass airdrop of autonomous guided parafoils. *J Guid Control Dyn* 2008; 31: 1123–1132.
3. Carter D, George S, Hattis P, et al. Autonomous large parafoil guidance, navigation, and control system design status. *AIAA Paper* 2007; 2514..
4. Carter D, George S, Hattis P, et al. Autonomous guidance, navigation, and control of large parafoils. *AIAA Paper* 2005; 1643: 23–26.
5. Carter D, Singh L, Wholey L, et al. Band-limited guidance and control of large parafoils. *AIAA Paper* 2009; 2981.
6. Kaminer II and Yakimenko OA. Development of control algorithm for the autonomous gliding delivery system. In: *17th AIAA Aerodynamic Decelerator Systems Technology Conference and Seminar*, Paper Number AIAA 2003-2116, Monterey, CA, 19–22 May 2003. Defense Technical Information Center.
7. Murray JE, Sim AG, Neufeld DC, et al. *Further development and flight test of an autonomous precision landing system using a parafoil*. Vol. 4599. NASA Technical Memorandum 4599, Dryden Flight Research Facility, CA: National Aeronautics and Space Administration, Office of Management, Scientific and Technical Information Program, 1994.
8. Slegers NJ and Yakimenko OA. Optimal control for terminal guidance of autonomous parafoils. In: *20th AIAA Aerodynamic Decelerator Systems Technology Conference and Seminar*, Paper Number AIAA 2009-2958, Seattle, WA, 4–7 May 2009. Defense Technical Information Center.
9. Calise A and Preston D. Design of a stability augmentation system for airdrop of autonomous guided parafoils. *AIAA Paper* 2006; 6776..
10. Ward M, Costello M and Slegers N. On the benefits of in-flight system identification for autonomous airdrop systems. *J Guid Control Dyn* 2010; 33: 1313–1326.
11. Ward M, Costello M and Slegers N. Specialized system identification for parafoil and payload systems. *J Guid Control Dyn* 2012; 35: 588–597.
12. Yakimenko OA, Slegers NJ and Tiaden RA. Development and testing of the miniature aerial delivery system snowflake. In: *20th AIAA Aerodynamic Decelerator Systems Technology Conference and Seminar*, Paper Number AIAA 2009-2980, Seattle, WA, 4–7 May 2009. Defense Technical Information Center.

13. Masters FJ, Vickery PJ, Bacon P, et al. Toward objective, standardized intensity estimates from surface wind speed observations. *Bull Am Meteorol Soc* 2010; 91: 1665–1681.
14. Antoniou I, Courtney MS, Ejsing Jørgensen H, et al. Remote sensing the wind using lidars and sodars. In: *Conference proceedings (online) Brussels. European Wind Energy Association (EWEA)*, 2007.
15. Krishnamurthy R, Calhoun R, Billings B, et al. Wind turbulence estimates in a valley by coherent Doppler Lidar. *Meteorol Appl* 2011; 18: 361–371.
16. Milton Huffaker R and Hardesty R. Remote sensing of atmospheric wind velocities using solid-state and co 2 coherent laser systems. *Proc IEEE* 1996; 84: 181–204.
17. Herrmann TA, Ward MB, Costello M, et al. Utilizing ground-based LIDAR for autonomous airdrop, ser. In: *AIAA Aerodynamic Decelerator Systems (ADS) Conference, Aerodynamic Decelerator Systems Technology Conferences*, Paper Number 2013-1387, Daytona beach, FL, 2013. American Institute of Aeronautics and Astronautics.
18. Goodrick TF and Murphy A. Analysis of various automatic homing techniques for gliding airdrop systems with comparative performance in adverse winds. In: *Fourth aerodynamic deceleration systems conference*, Paper Number 1973-462, Palm Springs, CA, 1973. American Institute of Aeronautics and Astronautics.
19. Jann T. Advanced features for autonomous parafoil guidance, navigation and control, ser. In: *18th AIAA Aerodynamic Decelerator Systems Technology Conference and Seminar, Aerodynamic Decelerator Systems Technology Conferences*, Paper Number 2005-1642, Munich, Germany. American Institute of Aeronautics and Astronautics.
20. Dubins LE. On curves of minimal length with a constraint on average curvature, and with prescribed initial and terminal positions and tangents. *Am J Math* 1957; 79: 497–516.
21. Ward M. *Adaptive glide slope control for parafoil and payload aircraft*. Dissertation, School of Aerospace Engineering, Georgia Institute of Technology, 2012.
22. Slegers N, Beyer E and Costello M. Use of variable incidence angle for glide slope control of autonomous parafoils. *J Guid Control Dyn* 2008; 31: 585–596.
23. *Military Standard, Flying Qualities of Piloted Aircraft*, Mil-std-1797a ed., 1990.
24. Brown GJ. Parafoil steady turn response to control input. *AIAA Paper* 1993; 1241: 10–13.